

## Article

# Log Transformed Coherency Matrix for Differentiating Scattering Behaviour of Oil Spill Emulsions Using SAR Images

Kinjal Prajapati <sup>1</sup>, Ratheesh Ramakrishnan <sup>2</sup>, Madhuri Bhavsar <sup>1,\*</sup>, Alka Mahajan <sup>3</sup>, Zunnun Narmawala <sup>1</sup>, Archana Bhavsar <sup>4</sup>, Maria Simona Raboaca <sup>5,\*</sup> and Sudeep Tanwar <sup>1,\*</sup>

- <sup>1</sup> Department of Computer Science and Engineering, Institute of Technology, Nirma University, Ahmedabad 382481, India; 19PTVPHDE201@nirmauni.ac.in (K.P.); zunnun.narmawala@nirmauni.ac.in (Z.N.)  
<sup>2</sup> Space Application Center, ISRO, Ahmedabad 380015, India; ratheeshr@sac.isro.gov.in  
<sup>3</sup> SVKM's Mukesh Patel School of Technology, Management, and Engineering, Mumbai 400056, India; alka.mahajan@nmims.edu  
<sup>4</sup> Department of Computer Engineering, SSBT'S College of Engineering and Technology, Bambhori, Jalgaon 425001, India; asgujar@rediffmail.com  
<sup>5</sup> National Research and Development Institute for Cryogenic and Isotopic Technologies—ICSI Râmnicu Valcea, Uzinei Street, No. 4, P.O. Box 7 Raureni, 240050 Râmnicu Vâlcea, Romania  
\* Correspondence: madhuri.bhavsar@nirmauni.ac.in (M.B.); simona.raboaca@icsi.ro (M.R.S.); sudeep.tanwar@nirmauni.ac.in (S.T.)

**Abstract:** Oil spills on the ocean surface are a serious threat to the marine ecosystem. Automation of oil spill detection through full/dual polarimetric Synthetic Aperture Radar (SAR) images is considered a good aid for oil spill disaster management. This paper uses the power of log transformation to discern the scattering behavior more effectively from the coherency matrix (T3). The proposed coherency matrix is tested on patches of the clean sea surface and four different classes of oil spills, viz. heavy sedimented oil, thick oil, oil-water emulsion, fresh oil; by analyzing the entropy ( $H$ ), anisotropy ( $A$ ), and mean scattering angle alpha ( $\alpha$ ), following the  $H/A/\alpha$  decomposition. Experimental results show that not only does the proposed T3 matrix differentiate between Bragg scattering of the clean sea surface from a random scattering of thick oil spills but is also able to distinguish between different emulsions of oil spills with water and sediments. Moreover, unlike classical T3, the proposed method distinguishes concrete-like structures and heavy sedimented oil even though both exhibit similar scattering behavior. The proposed algorithm is developed and validated on the data acquired by the UAVSAR full polarimetric L band SAR sensor over the Gulf of Mexico (GOM) region during the Deepwater Horizon (DWH) oil spill accident in June 2010.

**Keywords:** oil spill detection; UAVSAR; Deep Water Horizon; weathered oil; oil characterization; SAR Polarimetry

**MSC:** 49M27; 54B15



**Citation:** Prajapati, K.; Ramakrishana, R.; Bhavsar, M.; Mahajan, A.; Narmawala, Z.; Bhavsar, A.; Raboaca, M.S.; Tanwar, S. Log Transformed Coherency Matrix for Differentiating Scattering Behaviour of Oil Spill Emulsions Using SAR Images. *Mathematics* **2022**, *10*, 1697. <https://doi.org/10.3390/math10101697>

Academic Editor: Adrian Olaru

Received: 2 April 2022

Accepted: 13 May 2022

Published: 16 May 2022

**Publisher's Note:** MDPI stays neutral with regard to jurisdictional claims in published maps and institutional affiliations.



**Copyright:** © 2022 by the authors. Licensee MDPI, Basel, Switzerland. This article is an open access article distributed under the terms and conditions of the Creative Commons Attribution (CC BY) license (<https://creativecommons.org/licenses/by/4.0/>).

## 1. Introduction

During the last few decades, oil spills on the ocean surface, either accidental or deliberate discharges by ships, have grown with the increase in maritime transportation. It has been estimated that 457,000 tonnes of oil are released by shipping or accidents into the ocean every year [1]. Several oil spill accidents have been reported in the last few years, from the Deepwater Horizon oil spill in the year 2010, with 134 million gallons of oil spilled into the ocean, to the Mauritius oil spill in the year 2020, with 1200 tones of oil spilled into the ocean, leaving huge and long-lasting damage on the marine life and coastal region. Developing a cost-effective oil spill detection system has been the subject of research for the past two decades [2–5] for contingency planning, mitigation, and remediation to save the marine ecosystem from toxic oils.

Oil slicks can spread quickly on the sea surface through transportation both horizontally on the surface and vertically within the water column. After the oil spill, the

weathering effects such as evaporation, emulsification, submerged oil sinking, dispersion, sedimentation, dissolution, oil-mineral aggregation, photolysis, etc. can cause a loss of material through the evaporation or concentration of material into emulsions that can persist for a long time in the environment [6,7]. The oil spill may drift on the sea surface for many days, weeks, or even months, during which its chemical composition changes due to weathering [8]. Hence, to reduce or clean the oil spill, one needs to know its source, the spill extent, the estimate of the quantity, the range of probable transport paths, and current and future meteorological and sea conditions.

State-of-the-art remote sensing technologies with various sensors such as optical, infrared, thermal, microwave, etc., have been successfully used for effective data acquisition of oil spill [9]. Each sensor has proved its capabilities for efficient oil spill detection over the ocean surface, but each has its limitations. For example, optical sensors are limited to image acquisition during cloud coverage and daylight dependency. Microwave SAR sensors provide a potential alternative due to their all-weather and day-night imaging capability [10,11]. Oil spill detection using SAR data was carried out using single polarimetric SAR data using dark spot detection. However, with the development of multi-polarized SAR images, oil spill detection was much improved [12]. The multi-polarimetric SAR data have phase information and amplitude and intensity, which helps in a detailed analysis of the image resulting in better classification and discrimination of the type of oil spill. Promising technologies without a rapid response capability were largely not useful during the spill, although important data were collected for post-spill interpretation.

### 1.1. Motivation

An oil spill on the ocean surface not only pollutes the ocean water but also has adverse effects on the marine ecosystem and coastal region; hence, the major objective of oil spill detection and characterization is immediate dissipation of the oil spill information to the rightful stakeholder for the mitigation process. In response to a spill, accurate and rapid information on spill magnitude, location, and spread enables more effective and efficient cleanup, reducing the impact of oil spills on the marine ecosystem and cleanup cost. Most effective techniques for oil spill mitigation other than manual cleanup include oil booms, skimmers, sorbents, dispersants, burning in-situ, bio-remediation, and chemical stabilization. Here the type of sorbents, dispersants, and bio-remediation and chemical stabilization techniques are dependent on the chemical composition of the identified oil spill. Hence, the major issue with the existing offshore oil pollution treatment is the lack of information about the type of oil spill, amount of oil spill, and spread area. The majority of the research work has defined and successfully implemented various approaches for oil spill detection on the ocean surface. Still, comparatively least efforts have been made for the characterization of oil spill based on their physical and chemical properties that varies based on the weathering effect. Here in our research work, we propose a log transformation approach that can help estimate the physical-chemical properties of the oil spill based on the thickness and weathering using remote sensing SAR data which can be further used for effective cleanup and mitigation process by offshore pollution treatment authorities.

Various remote sensing technologies are analyzed together to address the rapid response to oil spill detection, including the type of oil spill and weathering effect on the oil spill. Oil spill detection using a single polarized SAR image aims toward identifying dark spots in the image due to reduced back scattered area generated due to dampening of small capillary and gravity waves over the oil-covered area. However, other than oil spills, various other oceanic phenomena result in low backscatter area and thus generating look-alikes of the oil spill in the image [8,13]. Various ancillary data from other sensors, geometric and contextual features of low backscattered areas can help to categorize dark formations into oil spills and look-alikes with high confidence [14,15]. Studies show that due to strong reliance on the suitable threshold, number of training samples, and ancillary data, single polarized SAR images are used in limited capacity. Further, the majority of research work is focused on oil spill detection with minimal emphasis on characterization of oil spill based

on weathering effect on oil spill resulting into change physical and chemical properties of the oil. Moreover, differentiation between different emulsions of oil spills and their physical-chemical characteristics is difficult using the optical and single polarimetric SAR data. Hence, the use of multipolarimetric SAR data is much preferred for better classification and characterization of various types of the oil spill. Rapid Response Products were key to response utilization data needs are time-critical; thus, a high technological readiness level is critical to the operational use of remote sensing products such as multipolarimetric SAR data.

### 1.2. Novelty and Scientific Contribution

In this paper, the log transformation over the coherency matrix followed by eigenvalue-eigenvector based  $H/A/\alpha$  decomposition of SAR image for efficient oil spill detection and characterization of various types of oil is used. Extensive research has already been conducted for efficient oil spill detection using various remote sensing data [7,8,16,17] but comparatively less research has been conducted on studying and discriminating the type of weathered oil [18,19]. The majority of the research work on SAR images for oil spill detection until now has been carried out on the coherency matrix T3 followed by the decomposition algorithm. Here in our case, we propose to apply the log transformation on the building pillars of polarimetric images, i.e., its Coherency Matrix T3. We have applied the log transformation on each element of the T3 matrix which has shown a major impact on the standard decomposition algorithm, which takes the T3 matrix as input for further processing. Here we have used the well renowned  $H/A/\alpha$  Decomposition algorithm for oil spill detection [20,21], but the discriminating type of oil spill was difficult here. The proposed log transformation over the coherency matrix obtained from the input UAVSAR full polarimetric has shown extraordinary effect in the discrimination of weathered oil. The  $H/A/\alpha$  decomposition using the proposed log-transformed coherency matrix effectively detects and discriminates the type of weathered oil spill and highlights the minor features of the image with unique signatures as compared to traditional  $H/A/\alpha$  decomposition. Further, this log-transformed T3 can be used to derive other traditionally established polarimetric parameters and another decomposition algorithm as per requirement.

Various chemical, physical and biological processes on the oil spill plays a significant role in the spread and behavior of oil spill on the ocean surface. The DWH oil spill continued from April 2010 to August 2010 with a time span of 84 days. During this period, the oil spill has undergone various physical and chemical degradation (weathering) and emulsification with water. To relate the DWH oil spill signature, researchers have collected the samples of the various types of oil, including weathered oil, from different locations (i.e., surface oil and oil collected at coastal regions) of DWH oil spill at a fixed interval of time. In [22], the chemical composition of weathered oil of DWH oil spill incident was analyzed where collected emulsified oil samples during the spill period (May 2010), and they found it resolved n-alkanes  $\geq$  C14 compared to our samples which had an average of C13 n-alkanes. Moreover, in [23] analysis of n-alkane and PAH concentrations showed that four of the post-capping samples were less weathered than the six pre-capping samples. The trajectory map of oil spill spread can be generated using the physical and chemical properties of the oil spill. In [24] researchers developed the model that predicted locations and amounts of shoreline oiling were compared to the documentation of stranded oil by shoreline assessment teams. The model-estimated daily average water surface area affected by floating oil  $>1.0$  g/m<sup>2</sup> was 6720 km<sup>2</sup>, within the range of uncertainty for the 11,200 km<sup>2</sup> estimate based on remote sensing for DWH oil spill. In [18], the researchers carried out Lab Testing in the OHMSETT lab to evaluate the signatures of optical, thermal, and SAR sensors concerning various thicknesses and chemical composition of the oil spill. They compared the results with the DWH oil spill results for analyzing relativity with real-time events. Hence extensive study on the physical and chemical composition of weathered oil and its significant signature over SAR images has been performed in the literature. Hence, the proposed approach for oil spill characterization based on weathering effect can be further

evaluated and combined with the available ground truth information as a base for future oil spill characterization for further research and prediction of physical-chemical properties of oil spill.

### 1.3. Organization

In this research paper, an effort has been made to detect oil spills on the ocean surface and distinguish the various types of weathered oil-based using the full polarimetric L-band SAR data with high accuracy. The State-of-Art of the oil spill detection using SAR Polarimetry which includes various approaches carried out by the renowned researcher has been discussed in Section 2. Further, the proposed log transformation over the coherency matrix has been discussed in detail in Section 3. The input L band full polarimetric UAVSAR dataset is discussed in Section 3.1. The significance of Log transformation over the coherency matrix of SAR image for oil spill detection is explained in Section 3.2. The detailed experimentation of the proposed approach carried out has been discussed in Section 4. The impact of the proposed log-transformed T3 for oil spill detection is tested using the  $H/A/\alpha$  decomposition, and its comparison with the conventional approach is presented in Section 4.2. The statistical analysis and accuracy assessment of the proposed approach using SVM classification is discussed in Section 4.3. Finally, the research work has been concluded with future work in Section 5.

## 2. State-of-the-Art

Traditionally oil spill on the ocean surface was detected based on the dark spot signature using various remote sensing sensors such as optical, thermal, Single Polarimetric SAR data [9]. Further, the ability of multi-polarized SAR technology to record multiple polarization responses of the scatterer and thereby help in studying and understanding their scattering behavior has led to an increase in usage of multi polarized images in several application areas along with oil spill detection. Figure 1 shows the fundamental steps involved in polarimetric SAR data processing for oil spill detection. Here, the input Single Look Complex/Multi Look Complex image is transformed into the second-order descriptors such as  $3 \times 3$  Hermitian average coherency (T3) and covariance (C3) matrices, which are further decomposed into independent scattering descriptors using the incoherent decomposition algorithms such as the Freeman [25,26], the Huynen, and the Eigenvector-eigenvalue decomposition [20,21], etc. for better physical interpretation. A broad number of polarimetric features such as entropy, anisotropy, scattering angle, degree of polarization, correlation coefficient, pedestal height, etc. [19,27,28] are then extracted from the decomposed components, which are feed into the supervised or unsupervised classifier for oil spill detection and characterization resulting into discrimination of oil spill from water and lookalikes.

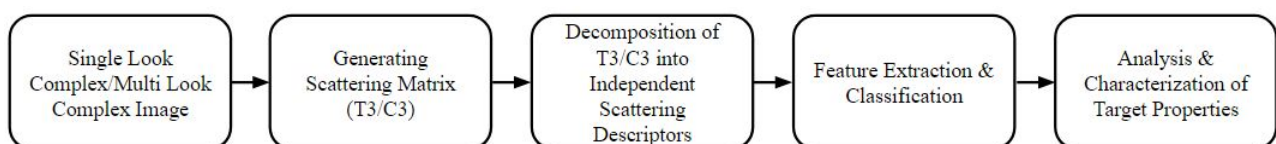


**Figure 1.** Flow of Multi-Polarized SAR Image Processing.

Various research works have been reported in the literature, which talk about different methodologies to detect oil spills using single and multi polarized SAR images [8,16,29]. A summary of a few recent research work relevant to the usage of optical and SAR data for oil spill detection and classification is discussed in Table 1. The significance of the polarimetric features such as Backscattered Intensity (span), Entropy ( $H$ ), Anisotropy ( $A$ ), Conformity Coefficient ( $\mu$ ), Pedestal Height ( $P$ ), mean scattering angle ( $\alpha$ ) for efficient oil spill detection were demonstrated in various research articles [28,30]. It was further observed that joint use of multiple fully polarimetric features as input to the classifier could provide higher accuracy than single fully polarimetric features [31]. In our recent work [32],

the selective polarimetric features of Pauli and  $H/A/\alpha$  decomposition were combined for efficient oil spill detection and discrimination of oil spill from lookalikes.. However, very few papers have tested the sensitivity of SAR to discriminate between oil slicks of different thicknesses and at different weathering/emulsification stages. For example, Jones, Holt, and Minchew in [7,33,34] have shown the effectiveness of L-band Airborne UAVSAR radar in detecting oil and differentiating mixed/weathered oil concentrated in the bay area from freshly released oil. The author of [18] experimented at the OHMSETT Lab environment for using optical as well as SAR sensors for the identification of various thicknesses of oil spill. Then, Singha in [35] investigated the use of fully polarimetric space-borne C (RADARSAT-2) and X (TERASAR-X) band images to decaffeinate between look-alike, emulsion, crude oil, and ocean water by developing ANN-based classifier; They have used 10 polarimetric features reported in the literature [27] were used to study their capability in distinguishing classes and showed that Scattering Diversity, Surface Scattering Fraction and Span features are more suitable.

**Table 1.** Summary of recent research on oil spill detection using SAR Polarimetry.

Ref.	Dataset	Approach	Objective and Outcome
[8]	Envisat ASAR, ERS-1 ERS-2, AVHRR	Oil spill Detection and Lookalike Discrimination	<ul style="list-style-type: none"> <li>Parameters used Normalized Radar Cross-Section, position and texture of spill, Co-polarized Phase difference, radar backscatter, image intensity, Dielectric constant.</li> <li>Supporting Ancillary data such as surface temperature, wind speed, chlorophyll content used.</li> </ul>
[30]	RadarSat-2	Oil Spill Detection and Classification	<ul style="list-style-type: none"> <li>Optimization of the Back-propagation Neural Network Classifier to Optimized Wavelet Neural Network</li> <li>Polarimetric features used : <math>(H), (A), (\mu), (P), (\alpha)</math>, Backscattered Intensity(SPAN).</li> </ul>
[7]	Full Pol UAVSAR	Oil Spill Thickness discrimination	<ul style="list-style-type: none"> <li>Type of oil analysed-Weathered Oil, oil penetrated into the coastal wetlands and inter-coastal waterways based on Variation in the intensity of the radar backscatter</li> <li>Effect of Incidence angle on radar properties of oil and water</li> <li>Average Intensity and Anisotropy at incidence angle <math>\angle 45^\circ</math> to <math>50^\circ</math> are better suited for discrimination of thickness of oil spill as compared to Entropy.</li> </ul>
[18]	UAVSAR, RADARSAT-2, Worldview-2	Oil Spill Thickness Classification	<ul style="list-style-type: none"> <li>OHMSETT Lab Experimental study on vivid signature of SAR and Optical sensors for different thickness of oil</li> <li>Accuracy assessment using Maximum Likelihood classifier</li> </ul>
[36]	Dual-Pol TerraSAR-X	Oil spill detection and Lookalike Discrimination	<ul style="list-style-type: none"> <li>Use of Combination of Traditional and Polarimetric Features for oil spill detection and discrimination from lookalike</li> <li>Features used-<math>H, A, \alpha, \mu, \sigma</math>, min contrast, max contrast, Span etc.</li> <li>The feature combination Surface scattering diversity, surface scattering fraction and Span was observed to have better accuracy of 90% using SVM classifier</li> </ul>
[37]	C Band Sentinel-1	Oil Spill detection and Segmentation using Deep Learning	<ul style="list-style-type: none"> <li>Analysis of oil spill detection using semantic segmentation using various deep learning architectures such as UNet, LinkNet, PSPNet, DeepLabv2, and DeepLabv3+.</li> <li>DeepLabv3+ was observed to have better performance for oil spill detection and discrimination from lookalikes.</li> </ul>
[28]	Radarsat-2, UAVSAR	Oil spill detection and Lookalike Discrimination	<ul style="list-style-type: none"> <li>Combination of proposed self similarity feature with 7 polarimetric features, i.e., <math>p, DoP, A_{12}, V, \mu, R_{CO}</math>, etc.</li> <li>Random Forest Classifier and Combination of DeepCNN with Superpixel Classification (Accuracy achieved-92.99% and 82.25% for each dataset)</li> <li>J-M Distance and F1 score for accuracy assessment</li> </ul>

Table 1. Cont.

Ref.	Dataset	Approach	Objective and Outcome
[19]	RADARSAT 2	Oil Spill Classification based on thickness	<ul style="list-style-type: none"> <li>• Discrimination of oil based on thickness using various combination of <math>H, A</math> and proposed <math>A_{12}</math> polarimetric parameters.</li> <li>• Accuracy assessment using parameters such as Michelson Contrast, J-M Distance and Random Forest Classification</li> </ul>
[38]	RADARSAT-2	Impact of seasons on oil spill detection	<ul style="list-style-type: none"> <li>• 6 Machine Learning approaches such as ANN, RF, Decision Tree, NavieBayes, LDA and Logistic Regression studied.</li> <li>• Impact of seasons i.e. Winter, Fall, Summer, Spring for acquiring oil spill image and prediction of source of oil spill (natural or anthropic)</li> <li>• Best case-winter season with Random Forest classifier</li> </ul>
[39]	Deep SAR Oil Dataset	Oil Spill Segmentation using CBD-Net	<ul style="list-style-type: none"> <li>• Approach to improve the feature representation of complex oil spills in SAR images using proposed CBD-Net edge detection algorithm.</li> <li>• Proposed manually generated Deep SAR Oil dataset.</li> </ul>
[40]	ERS SAR, ENVISAT 2 SAR	Feature Selection for efficient Oil spill Detection	<ul style="list-style-type: none"> <li>• Comparison of 5 feature selection method Correlation-based feature selection (CFS), Consistency-based filter, Information Gain, ReliefF and Recursive Feature Elimination for Support Vector Machine (SVM-RFE).</li> <li>• Selected Feature Evaluated using SVM Classification</li> <li>• 5 features SVM-RFE showed best feature selection with 87.1% classification accuracy</li> </ul>
[41]	RADARSAT-2, SIR-C/X SAR	Oil spill Detection	<ul style="list-style-type: none"> <li>• Use of Polarimetric Decomposition, i.e., <math>H/A/\alpha</math>, Yamaguchi-4 Component, Freeman-Durden</li> <li>• Polarimetric Parameters-SERD, <math>\mu</math>, Corelation Coefficient</li> <li>• SLIC superpixel segmentation with CNN classification</li> </ul>

The classification of remote sensing data is daunting as most of the supervised classification methods require a sufficiently large number of training samples along with well-verified test samples. Moreover, receiving the well-calibrated remote sensing data for oil spill incidents and the verified ground truth or ancillary data are critical. Still, Researchers have tried to use various supervised and unsupervised classification algorithms such as K-means clustering, maximum likelihood, Artificial Neural Network, Random forest, KNN, SVM, etc. for oil spill detection and discrimination for look alike [10,31,36,37]. The researcher in [38] evaluated the impact of 6 machine learning approaches such as ANN, RF, Decision Tree, Navie Bayes, LDA, Logistic Regression for effective oil spill detection and develops an algorithm for prediction of the best season for image acquisition of oil spill for Gulf of Mexico region. Among all traditional approaches, ANN and SVM have been majorly used by researchers for oil spill detection and characterization. Along with providing high accuracy with smaller training samples, SVM strikes the right balance between accuracy attained on a given finite amount of training patterns and the ability to generalize to unseen data. Its reported accuracy of SVM in oil spill studies ranges from 71% to 97% [10]. In [40], the authors have used five feature selection techniques by discarding irrelevant features for oil spill detection. These selected features are fed to the SVM classifier resulting in an accuracy of 87%. Hence, the SVM classification algorithm is majorly considered while dealing with remote sensing data, especially in the case of oil spill detection where there is a limitation of least availability input training samples leading towards the higher performance of the oil spill detection and classification for SAR Polarimetric data.

### 3. Proposed Approach

The flow of the proposed approach for identification and characterization of various types of the weathered oil spill is shown in Figure 2. The full polarimetric L band UAVSAR

data acquired near the Barataria Bay region of the Gulf of Mexico is used as input data. It includes various stages of weathered oil with verified ground truth. The input data set is first pre-processed to remove speckle noise using Refined Lee Filter. Further, the Hermitian Coherency (T3) matrix is generated using Stokes parameters obtained from the radar backscatter image. Additionally, the polarimetric decomposition is performed on the T3 matrix leading to the effective physical interpretation of the target object and classification. In the first phase, the standard polarimetric decomposition algorithms, i.e., eigenvalue-based decomposition algorithm,  $H/A/\alpha$  decomposition, are applied to the T3 matrix to study their efficiency in oil spill detection and discrimination of types of the oil spill. Here,  $H$  stands for entropy that signifies the randomness of the backscattering from the ocean surface,  $A$ , i.e., Anisotropy shows multiple backscattering behavior over the surface, and the mean scattering angle ( $\alpha$ ) defines the dominance of the specific scattering behavior over the surface. Finally, the same polarimetric decomposition algorithm is applied to the proposed log-transformed coherency matrix for enhanced oil spill discrimination especially discriminating the type of the weathered oil. The proposed approach is finally evaluated and analyzed using the various performance parameters such as Michelson Contrast, M-statistic, J-M distance and finally classification of weathered oil using SVM classification.

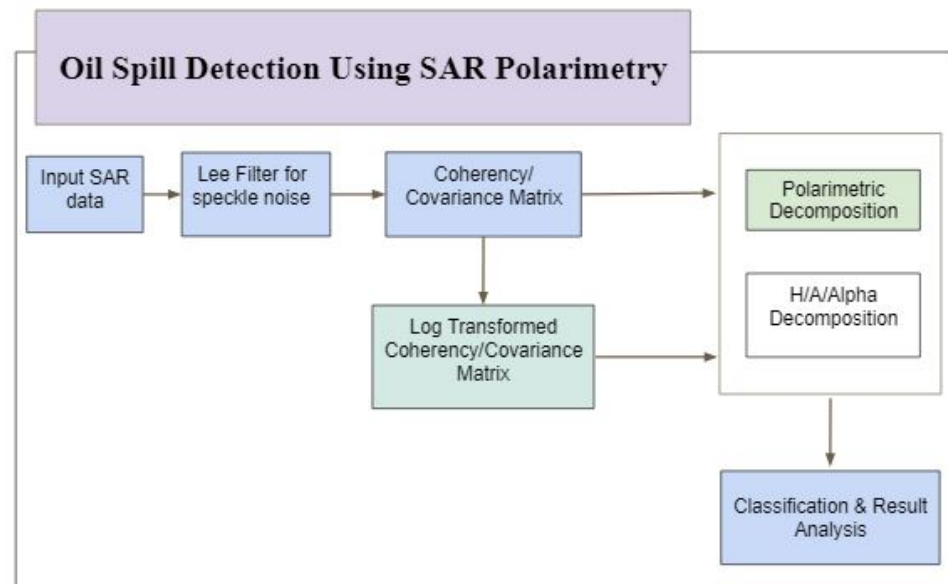


**Figure 2.** The proposed Log Transformation approach for efficient Oil Spill Detection using SAR Polarimetry.

### 3.1. Input Dataset

Following the Deepwater Horizon Oil spill disaster in the Gulf of Mexico (GoM) in April 2010 [42], NASA deployed the full polarimetric Uninhabited Aerial Vehicle Synthetic Aperture Radar (UAVSAR) L band radar to cover the oil affected areas of GoM and nearby coastal wetlands mainly in Barataria Bay (BB), Louisiana [33,43]. Images/Photographs captured by various space-borne and airborne sensors have shown large variations in slick properties in terms of thickness and states of weathering/emulsification over the large affected area [15]. The DWH oil spill continued from April 2010 to August 2010 with heavy spread over the ocean surface, while in the meantime, Oil slick processes on a day to week timescales, i.e., a typical oil spill response that includes horizontal and vertical transportation and surface diffusion, sedimentation and dissolution into the water column, emulsification, evaporation, and photochemical and biological degradation including weathering [9]. Along with the aerial photography, remote sensing sensors such as MODIS, LandsAT, AVIRIS, Sentinel, RadarSat, UAVSAR, etc. were used to capture the spread of the DWH oil spill [9,17,44] building a strong repository of the dataset with confirmed oil spill

and supporting ground truth and ancillary data. The researchers Cathleen Jones, B. Holt and team in [43] studied the signature of weathered oil transported to the coastal region of Barataria Bay (BB) using L UAVSAR data and ground truth data. The polarimetric features average intensity and entropy were used to analyze the impact of weathered oil over the BB coastal region, confirming the presence of weathered oil in the UAVSAR image as shown in Figure 3. Further, a detailed study on the characteristics of the weathered oil collected at BB during the DWH oil spill incident has been carried out by various researchers in [7,18,45].

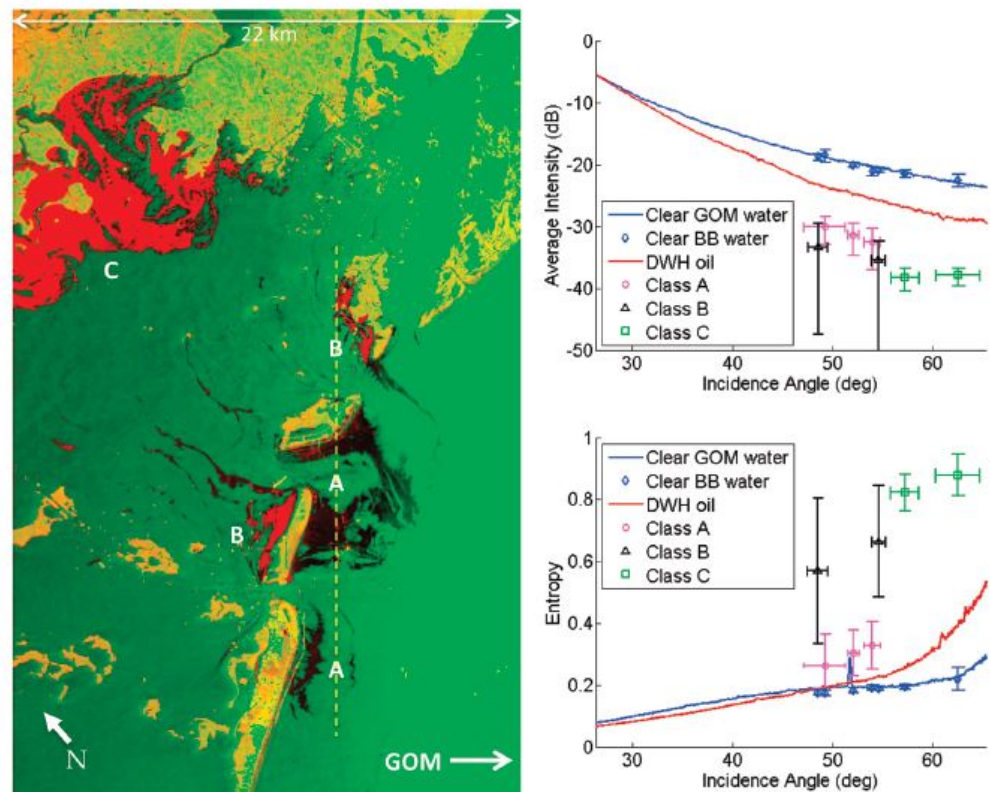


**Figure 3.** (left) Image with combination of Polarimetric features Average Intensity  $\Lambda$  (Red) and Entropy (Green) divided into 3 classes (A)–Thick Weathered oil, (B) Weathered oil mixed with Sediment near BB coastline and (C) Weathered oil heavily mixed with sediment. (Right)  $\Lambda$  (top) and entropy (bottom) plotted as a function of incidence angle for clean water in the GOM and in BB, oil in the main slick near the DWH site (DWH oil), and oil classes A, B, and C. [43].

As the aim is to study variations in oil characteristics due to differences in oil emulsification, the study of 3 images labeled A, B and C showed in Figure 4 are considered. Here, image A is the weathered oil image mentioned in Figure 3 is the includes an oil patch at various stages of weathering effect such as emulsion, weathered oil, and sedimented oil (mixed with sediment) as it was captured in June 2010 after 2 months of the oil spill. Image A also includes the oil transported over the coastal region, which by the time has undergone weathering effect and mixed with sediment after reaching coastline. Images B and C in Figure 4 cover the DWH rig site spotting the fresh released oil due to the removal of the containment cap. The presence of oil spill and its various stage of weathered oil were confirmed by researchers in [7,8]. Further, authors have estimated that the upper layer of the oil slick was a mixture of approximately 80% oil and 20% seawater, with a range in the volumetric oil concentration from 65% to 90% across the slick near the DWH site [15]. Figure 5a shows the combination of cropped part of images B and C of Figure 4 consisting of clean water and oil-contaminated water near the rig site labeled as fresh released oil.

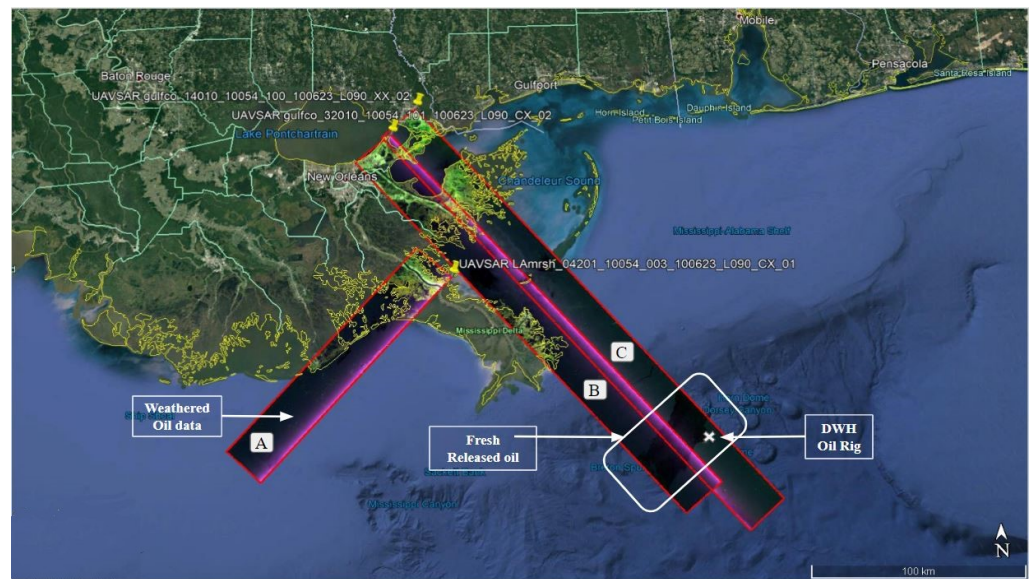


**Figure 4.** Study area: (B,C) UAVSAR L band multi-polarization images of main slick of DWH spill-gulfc0\_14010 (23 June 2010 20:42 UTC) and gulfc0\_32010 (23 June 2010 21:08 UTC). (A) UAVSAR multi-polarization images of Barataria Bay (BB), Louisiana and the barrier islands at the entrance to BB; BB is in the upper part of the image – Lamrsh\_04201 (23 June 2010 23:05 UTC). The colors are a composite of the HH-polarization intensity image (red), the VV (black) and the HV (green).

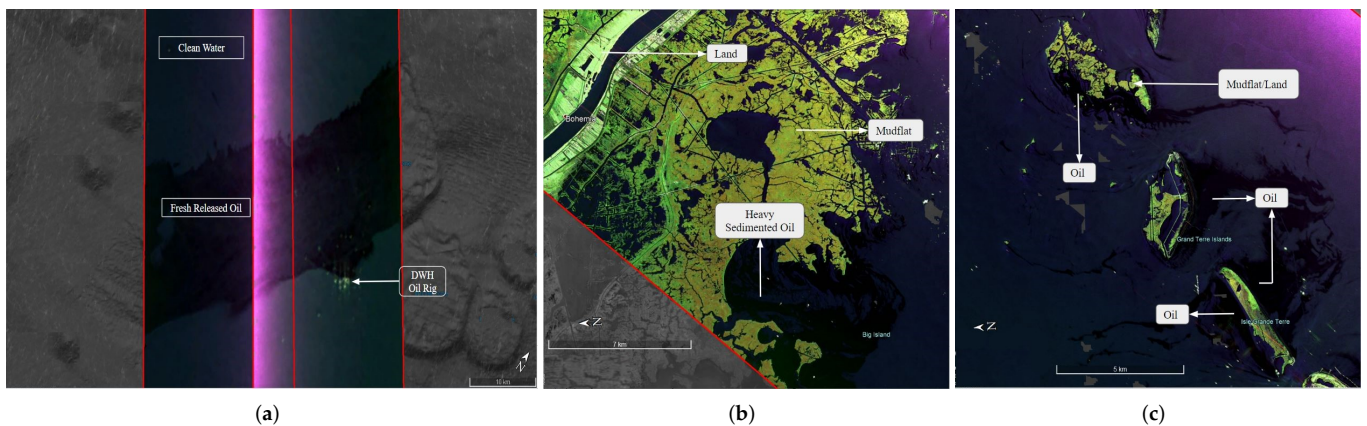


**Figure 5.** Patches of UAVSAR images considered in study: (a) shows surface oil and clean water near DWH rig site; (b) shows oil heavily mixed with sediment and other surfactants that has moved into the interior bay labeled as Heavy Sedimented Oil. (c) shows weathered oil on the GOM side of the barrier islands partially mixed with sediment labeled as oil [43].

Image A covers oil concentrated in coastal wetlands in BB and at barrier islands at the entrance to BB, which is believed to be several days older than the capture time. During this period, the oil’s chemical and physical properties may have changed due to weathering/emulsification, and the oil have mixed with suspended sediment and other surfactants near the shore, further altering its bulk physical properties [National Research Council, 2003]. Hence, to characterize all these variants of oil, two patches of image A in Figure 4 are taken as shown in Figures 5b,c representing different amount of emulsified oil, further verified in papers [33,43]. The patch labeled as heavy sedimented oil in Figure 5b is defined as weathered oil on the GOM side of the barrier islands, patch labeled as oil in Figure 5a is oil on the immediate bay side of the barrier islands that has partially mixed with sediment and other surfactants.

### 3.2. Significance of Log Transformed T3 Matrix

Log transformation of data has shown its successful applicability in various domains ranging from medical image processing in various linear regression models to satellite image processing. Depending on the type of data and application area, researchers have applied log transformation taking advantage of different facts such as: (i) it reduces skewness of the data and makes data fit as input in regressions, (ii) reduces multiplicative speckle noise into additive speckle in SAR image [46], (iii) compresses the dynamic range of data by enhancing lower intensity pixels which ultimately helps to improve the quality of satellite images to capture and analyze unseen features in the low-intensity region of the image clearly [47]. Log transformation increases the processing speed as it compresses the dynamic range of images with large variations in intensity values [48].

For fully polarimetric SAR data, the backscattering properties of the object are described using the backscattering matrix as given in Equation (1)

$$S = \begin{bmatrix} S_{HH} & S_{HV} \\ S_{VH} & S_{VV} \end{bmatrix} \tag{1}$$

where  $S_{XY}$  is the scattering component with  $x$  as transmit polarization and  $y$  as receive polarization. Here  $H$  stands for horizontal polarization while  $V$  stands for vertical polarization.

Since the oil spill in the SAR image appears as dark signatures as shown in Figure 5, the use of log transformation over the SAR image enhances and highlights the oil spill signatures in the input SAR image. Hence, this paper proposes using log-transformation on T3 matrix elements for oil spill characterization using SAR data. The conventional T3 matrix is shown in Equation (2), where the 3 diagonal elements represent the dominant scattering behavior, i.e., surface scattering, double-bounce scattering, and volume scattering, respectively. The log-transformed T3 is shown in Equation (3), where the log transformation is applied to each element of the T3 matrix, forming a new log transformed T3 matrix.

$$\langle [T] \rangle = \begin{bmatrix} \langle |S_{HH} + S_{VV}|^2 \rangle & \langle (S_{HH} + S_{VV})(S_{HH} - S_{VV})^* \rangle & 2\langle (S_{HH} + S_{VV})S_{HV}^* \rangle \\ \langle (S_{HH} - S_{VV})(S_{HH} + S_{VV})^* \rangle & \langle |S_{HH} - S_{VV}|^2 \rangle & 2\langle (S_{HH} - S_{VV})S_{HV}^* \rangle \\ 2\langle S_{HV}(S_{HH} + S_{VV})^* \rangle & 2\langle S_{HV}(S_{HH} - S_{VV})^* \rangle & 4\langle |S_{HV}|^* \rangle \end{bmatrix} \tag{2}$$

$$\langle [T^*] \rangle = \begin{bmatrix} \langle 10\log_{10}|S_{HH}+S_{VV}|^2 \rangle & \langle 10\log_{10}((S_{HH}+S_{VV})(S_{HH}-S_{VV})^*) \rangle & 2\langle 10\log_{10}((S_{HH}+S_{VV})S_{HV}^*) \rangle \\ \langle 10\log_{10}((S_{HH}-S_{VV})(S_{HH}+S_{VV})^*) \rangle & \langle 10\log_{10}(|S_{HH}-S_{VV}|^2) \rangle & 2\langle 10\log_{10}((S_{HH}-S_{VV})S_{HV}^*) \rangle \\ 2\langle 10\log_{10}(S_{HV}(S_{HH}+S_{VV})^*) \rangle & 2\langle 10\log_{10}(S_{HV}(S_{HH}-S_{VV})^*) \rangle & 4\langle 10\log_{10}(|S_{HV}|^*) \rangle \end{bmatrix} \tag{3}$$

Initially, during the statistical analysis of the elements of the T3 matrix, it was observed that the T3 element value range of each aspect, such as ocean water or oil, was very low. Here the identification of oil spill was possible, but discrimination of type of oil spill was difficult due to minor variation in pixel range value. It is found that the application of log transformation on each of 9 elements of the T3 matrix improvised the separability of the element range value for the vivid object of the image. For more clarity to the proposed idea, the histogram of diagonal elements (T11, T22, T33) of standard T3, as well as log-transformed T3 for the patch of water region of the image, was generated as shown in Figure 6. It is observed from Figure 6a,b The range of water for standard T3 elements, i.e., T11 (0.01 to 0.03), has improved from (−25 to −15) providing larger scope of separability for each object to be identified or discriminated.

The three obtained eigenvalues ( $\lambda_1, \lambda_2, \lambda_3$ ) are related to strength of three different scattering mechanisms namely surface scattering which is mainly observed in ocean surface; double-bounce scattering majorly observed in urban area, mudflats and man-made structures such as ships, buildings, etc.; volume scattering prominently seen in forests respectively. Figure 7 shows images of three eigenvalues computed using both conventional and log transformed T3 for a cropped input UAVSAR image A of Figure 4. The images i.e.,

Figure 7a,c,e correspond to eigenvalues computed using conventional T3 while other 3 images, i.e., Figure 7b,d,f correspond to eigenvalues computed using log transformed T3.

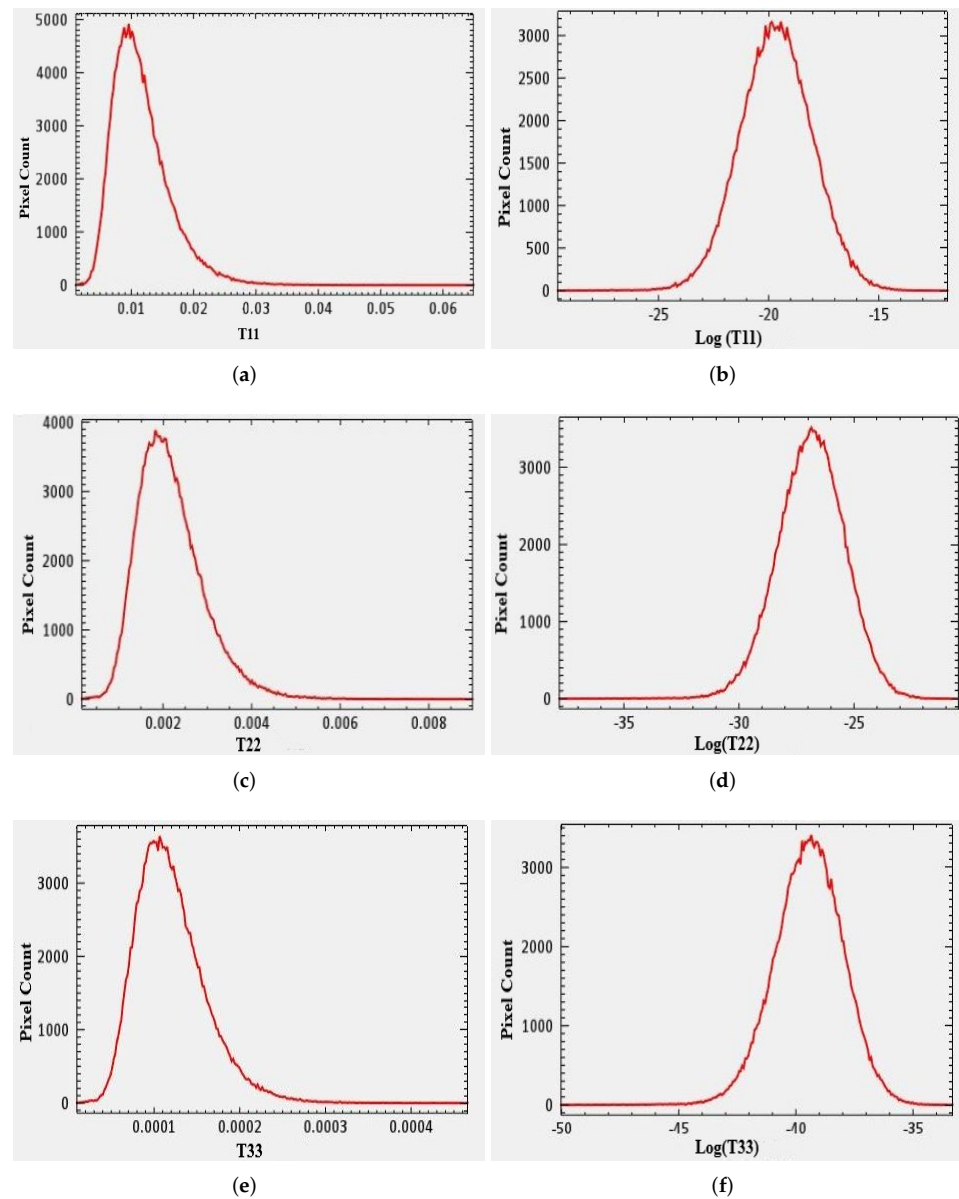


**Figure 6.** Histogram of elements of conventional T3 (a) T11, (c) T22, (e) T33 and Log transformed T3 (b,d,f) for a clean water patch.

The comparison and interpretation of images of respective eigenvalues are as follows:

- (i) It is observed from the  $\lambda_1$  computed using conventional T3 in Figure 7a and using log-transformed T3 in Figure 7b that oil slicks are clearly visible and easily distinguishable from surrounding water in log-transformed version as compared to the conventional version. In Figure 7a, all the features of the water and oil are suppressed in the dark region due to low backscatter, and the area of water and oil are not discriminated due to minor variation in their ranges. The log-transformed version gives superior results due to the enhancement of lower pixel values which enhances the ranges of oil and water in the image resulting in the proper visible distinction between oil and water in the image as shown in Figure 7a.
- (ii) Comparison of  $\lambda_2$  using conventional T3 and log-transformed T3 in Figure 7c,d has led to a very interesting and important observation: Image of  $\lambda_2$  of log-transformed T3 also

highlights slicks of oil along with mudflats and man-made houses present on along sides of canal structure seen at the top of the image. As the oil slicks present in these patches are mixed with sediments (refer Section 3.1) and thus exhibit double-bounce scattering along with surface scattering.  $\lambda_2$  of conventional T3 fails to capture this signature.

- (iii) Image of  $\lambda_3$  Figure 7f calculated using log-transformed T3 reveals no particular structure as there may not be any object present that exhibits volume scattering dominantly. Thus, a clear distinction of features is possible due to eigenvalues of log scaled T3, resulting in better discrimination among different emulsified slicks based on the calculated Entropy, Anisotropy, and Alpha angle.

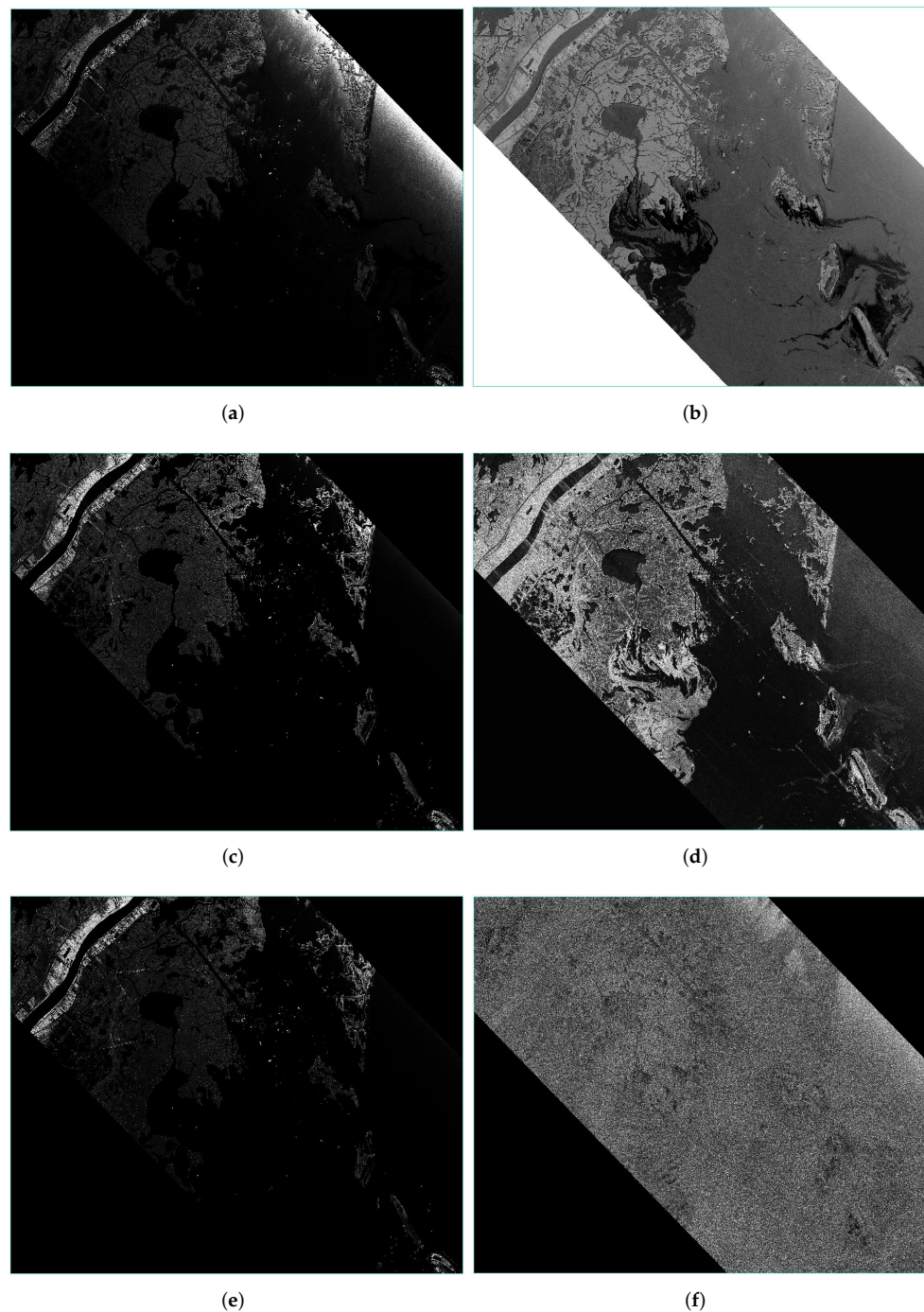


**Figure 7.** Comparative Analysis of Eigenvalues obtained form conventional T3, i.e., (a) T11, (c) T22, (e) T33 and Log Scaled T3 (b) T11, (d) T22, (f)T33.

### 3.3. H/A/α Decomposition

Further, to validate the effectiveness of log scaled T3 matrix, Eigen-value based H/A/α decomposition algorithm was applied using both conventional and log-transformed T3. The rotation invariant H/A/α parameters (Entropy, Anisotropy (A) and Scattering angle (α) are calculated based on the eigenvalues as shown in Equations (4)–(6), respectively [20].

$$H = - \sum_{i=1}^3 P_i \log_3 P_i \quad \text{with} \quad P_i = \lambda_i / (\lambda_1 + \lambda_2 + \lambda_3) \quad (4)$$

Entropy (4) value signifies the randomness in the backscattered radiation using pseudo probability of the eigenvalues  $P_i$ . Further, the amount of multiple backscattering behaviour of the target object is evaluated using anisotropy (A) which is calculated as (5)

$$A = \frac{\lambda_2 - \lambda_3}{\lambda_2 + \lambda_3} \quad (5)$$

The mean scattering angle  $\alpha$  shows the most dominant scattering behaviour of the target object signifying the presence of various type of objects in image, i.e., surface scattering for water, double bounce or volume scattering for metallic object such as ships on the ocean surface.

$$\bar{\alpha} = \sum_{i=1}^3 p_i \alpha_i \quad (6)$$

The resultant image of H/A/α decomposition using conventional T3 matrix for Deep Water Horizon oil spill incident image with various type of weathered oil confirmed by various researcher is shown Figure 8. Here H/A/α is taken as RGB components of the image where H stands for R component and similarly for A and α for G and B component respectively.

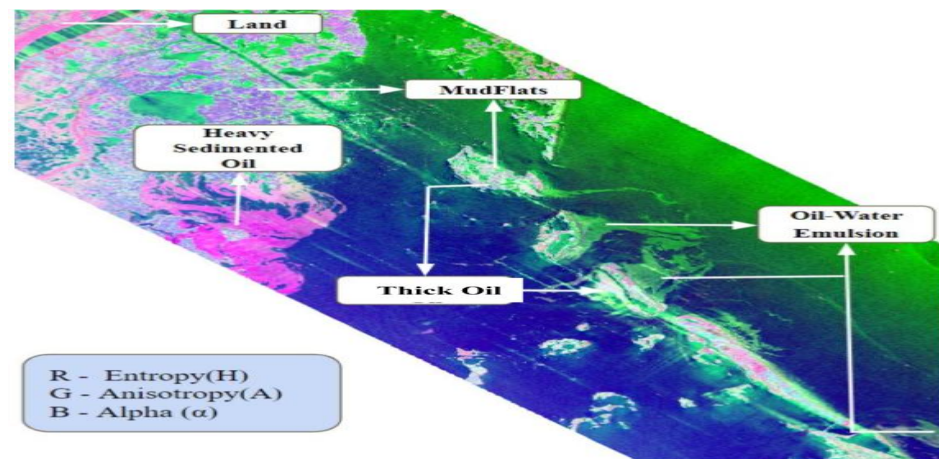


Figure 8. H/A/α decomposition using Conventional T3.

## 4. Experiments and Results Analysis

In this section we describe the experimental settings and performance analysis of the results obtained for detecting and characterization of oil spill using the proposed methodology.

### 4.1. Experimental Setup and Parameters

The L band full polarimetric SAR images for DWH oil spill incident consisting of various weathered oil and freshly released oil which is discussed in Section 3.1 has been used as input data. This quad pol UAVSAR data are fed as input to the PolSAR pro tool for speckle filtering (Refined Lee filter) for noise removal, followed by generation of Coherency

matrix T3 from the scattering matrix. This  $(3 \times 3)$  T3 matrix is generated for each image pixel, resulting in  $m \times n \times 9$  dimensions of the input data. A Matlab code is developed for the calculation of Eigen value-based polarimetric parameters Entropy ( $H$ ), Anisotropy ( $A$ ), and mean scattering angle ( $\alpha$ ) using this T3 matrix as input. In parallel to this, another Matlab code is generated to deploy the proposed log transformation of the T3 matrix followed by  $H/A/\alpha$  polarimetric decomposition. The evaluation of the effectiveness of the proposed log transformation approach has been performed using some well-established statistical analysis methods such as Michelson Contrast for target separability evaluation, M statistic for calculating the degree of discrimination and SVM classification for accuracy assessment of the proposed approach.

The performance parameters used for evaluation and comparison of the proposed log transformation methodology are described as follows

- Michelson Contrast (MC)

MC is one of the general criteria for evaluating target separability. It has thus been used to quantitatively define and evaluate contrasts between oil slicks and seawater under various polarimetric feature spaces [19]. MC is calculated as Equation (7).

$$MC = \frac{I_{max} - I_{min}}{I_{max} + I_{min}} \quad (7)$$

Here  $I_{min}$  and  $I_{max}$  indicate the maximum and minimum mean polarimetric feature values between the two target samples being tested, respectively, and the value range of MC is  $[0, 1]$ .

- M-Statistic (MS)

The MS assesses the degree of discrimination between the two-pixel groups. It operates by evaluating the separation between the histograms produced by plotting the frequency of all the pixel values within the two classes [49]. The M-statistic can be calculated using the mean  $\mu$  and standard deviation  $\sigma$  of two targets to be tested, respectively, as shown in Equation (8)

$$M = \frac{\mu_a - \mu_b}{\sigma_a + \sigma_b} \quad (8)$$

A value of  $M < 1$  denotes that the histograms significantly overlap and the ability to separate (or discriminate) the two regions is poor. A value of  $M > 1$  denotes that the histogram means are well separated and that the two regions are relatively easy to discriminate.

#### 4.2. $H/A/\alpha$ Decomposition Result Analysis

To assess the efficiency of log transformed coherency matrix in detecting and differentiating oil slicks of varying characteristics, variations in  $H/A/\alpha$  parameters have been calculated and analyzed using both conventional T3 and log transformed T3. Figures 9 and 10 shows the  $H/A/\alpha$  decomposition results of the identified cropped image consisting of fresh released surface oil and various types of weathered oil in Figure 5 of the UAVSAR dataset, using both conventional T3 and log transformed T3. The top three images, i.e., Figure 9a–c correspond to  $H/A/\alpha$  decomposition computed using conventional T3 while the bottom three images, i.e., Figure 9d–f corresponds to  $H/A/\alpha$  decomposition computed using log transformed T3. The results of image acquired near rig site with fresh released oil and clean water are shown in Figure 9a,b,d,e while the results of image acquired near BB consisting of various stage of weathered oil labeled as oil water emulsion, thick oil and heavy sedimented oil and land and mudflats are shown in Figures 9c,f and 10a,b.

It is observed from the Figure 9a,b that the signature of freshly released oil near the rig site labeled as fresh released oil is almost similar to water in the case of a conven-

tional approach while in the case of a log-transformed approach, the fresh released oil is distinguished signature as compared to water in Figure 9c,f.

However, due to similar backscattering behavior, the signature of thick oil and mudflats (pinkish white) in Figure 9c is getting mixed. At the same time, the oil-water emulsion (light-green) is quite distinguished from the conventional approach. However, in the case of the log-transformed approach, the oil-water emulsion, thick oil (dark red), and mudflats have clear, distinct signatures in Figure 9f. The  $H/A/\alpha$  decomposition result of another patch of image A in Section 3.1, consisting of weathered oil which is heavily mixed with sediment labeled as heavy sedimented oil, is shown in Figure 10. It is observed that the signatures of heavy sedimented oil (dark red) and land (light red) are different in the case of the log-transformed approach, while these signatures are getting mixed in the case of the conventional approach. Since the oil accumulated near the coast is heavily mixed with the sediment, the physical properties of the oil are changed such that the backscattering properties of heavy sedimented oil are similar to that of land in conventional  $H/A/\alpha$  decomposition. Hence, due to the enhancement of the dark features of oil using the log transformation, every minor feature or variation in the oil spill is captured, resulting in efficient oil spill detection and characterization. Other land features, such as mudflats, buildings and ships show clear, distinct features in the proposed log-transformed approach.

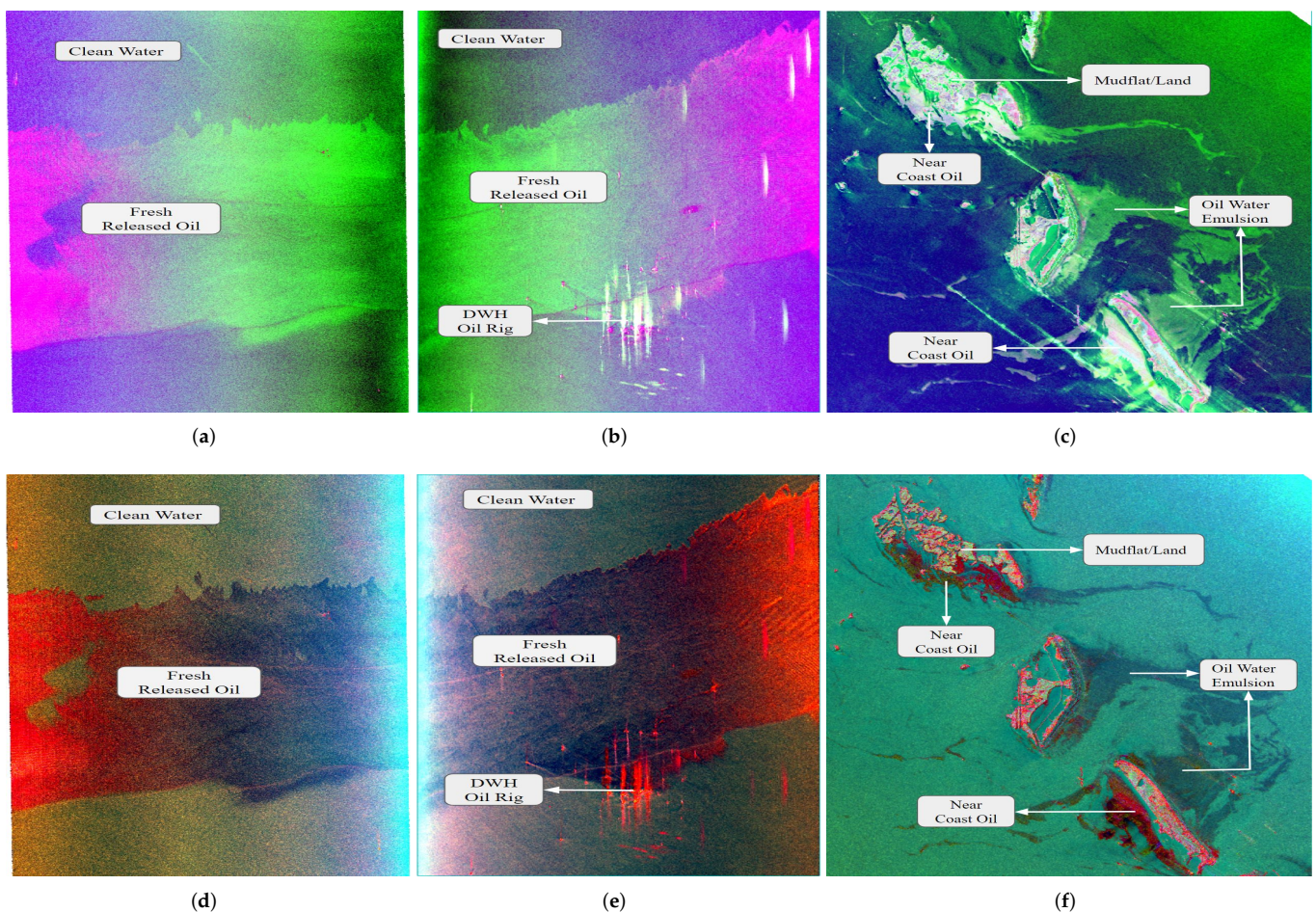


**Figure 9.** Comparative analysis of image generated using combination of entropy (red), anisotropy (green) and alpha (black) ( $H/A/\alpha$ ) using conventional T3 (a–c) and log transformed T3 (d–f) showing their capability in detecting and differentiating different emulsions of oil.

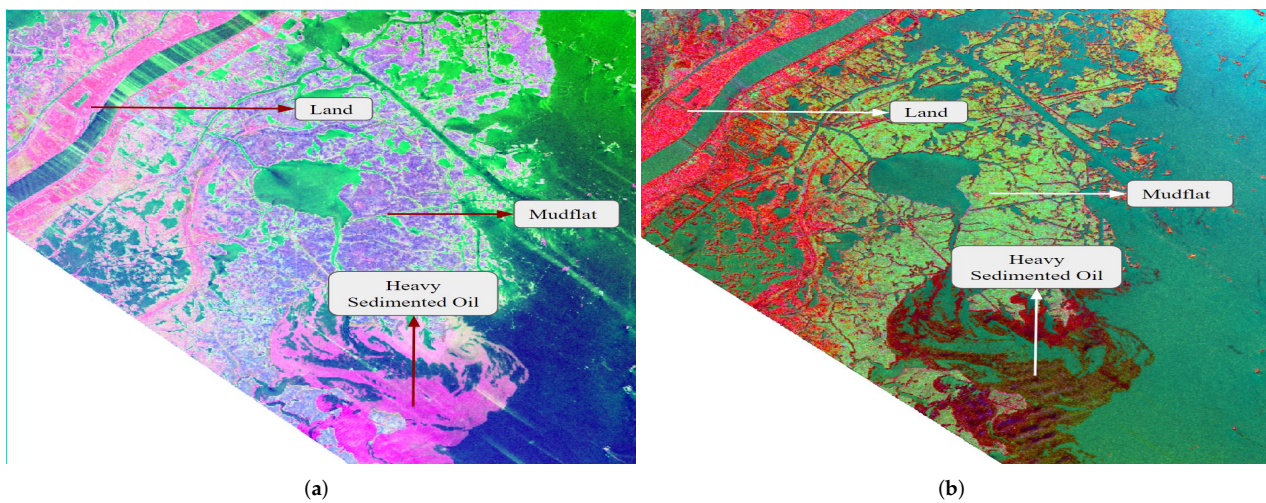


**Figure 10.** Comparative analysis of images generated by combining entropy (red), anisotropy (green) and alpha (black) ( $H/A/\alpha$ ) using conventional T3 (a) and log transformed T3 (b) showing their capability in differentiating between highly sedimented oil and mudflat/building.

Figure 11 shows the plots of entropy, anisotropy, alpha parameters calculated for different classes of oil emulsions (Oil-water Emulsion (red), thick Oil (Green), Heavy Sedimented oil (pink), Land/Mudflat (black)) for statistical analysis of the proposed approach. The observation from these plots are as follows.

- Entropy calculated using log-transformed T3 Figure 11d captures subtle contrast changes in oil-contaminated patches resulting due to different stages of emulsification which is not the case with entropy calculated using classical T3 Figure 11a. As shown in the histogram in Figure 11d, the oil-water emulsion has a range of 0.74 to 0.76 in the log-transformed approach. It can also differentiate between oil-water emulsion, thick oil, and heavy sedimented oil with an extended upper bound of the range. Further, the entropy values increase gradually from moderate weathering stage oil to high emulsified oil. However, the entropy range calculated using classical T3 Figure 11a for oil-water emulsion is 0.2 to 0.4, roughly which is the same as clean water and surface oil. This indicates that it does not differentiate between fresh and weakly weathered oil. Further, it also fails to capture minor changes in physical and electrical properties of thick oil and heavy sedimented oil as both have the same range. The blue line in the histogram is for a sample taken of mudflat/shrub/building present near Barataria Bay (BB), Louisiana. It can be clearly seen that the log-transformed T3 gives a different entropy range for highly mixed sedimented oil and mudflat/building regions even though both exhibit a similar scattering mechanism - moderate entropy double bounce. The separation between values of entropy for highly mixed sedimented oil and mudflat/building region is not that clear in the case of classical T3.
- Anisotropy values in Figure 11e calculated using log-transformed T3 show opposite behaviour than classical T3 in Figure 11b. Anisotropy calculated using log-transformed T3 has higher values for clean water and surface oil, which reduce from weakly emulsified oil to highly emulsified oil. However, the anisotropy values calculated using classical T3 cannot differentiate between clean water and any oil sample; it does not show a separate range for building/mudflat samples. On the other hand, anisotropy calculated using log-transformed T3 differentiates between clean water/surface water (Bragg scattering) from different emulsified oils (non-Bragg scattering). However, it fails to differentiate between building/mudflat and oil mixed with partial sediments.
- Alpha values Figure 11f calculated using log-transformed T3 do not show any favorable result in capturing differences between the type of scattering mechanism exhibited by water and different emulsified oils. It shows that clean water and all

kinds of oil samples were taken to follow the double bounce scattering. On the other hand, though, Alpha values Figure 11c calculated using classical T3 show surface scattering for clean water and surface oil; double-bounce scattering for oil mixed with sediments. However, it fails to differentiate between thick oil from surface oil/clean water and mudflat/building from oil mixed with sediments.

4.3. Statistical Analysis and Accuracy Assessment

It is observed from Figure 12 that the range of polarimetric features such as  $H$ ,  $A$ , and  $\alpha$  derived using conventional T3 are low (range from 0 to 0.45) for the majority of the cases while in the case of those derived using log-transformed T3 ranges from 0.2 to 0.8 on average. The important aspect observed here is the inseparability of some weathered oil observed for a conventional T3 approach such as emulsion and thick oil, thick oil and heavy sedimented oil, heavily sedimented oil and land shows a good separability in the case of the proposed log-transformed approach, respectively.

It is observed from Figure 13 that the range of polarimetric features such as  $H$ ,  $A$ , and  $\alpha$  derived using conventional T3 are low (range  $-0$  to 3) for the majority of the cases while in the case of those derived using log-transformed T3 ranges from 3 to 10 on average. The important aspect observed here is the inseparability of some type of weathered oil observed for conventional T3 approach such as emulsion and thick oil, thick oil and heavy sedimented oil, heavily sedimented oil and land shows good discrimination in the case of the proposed log-transformed approach, respectively.

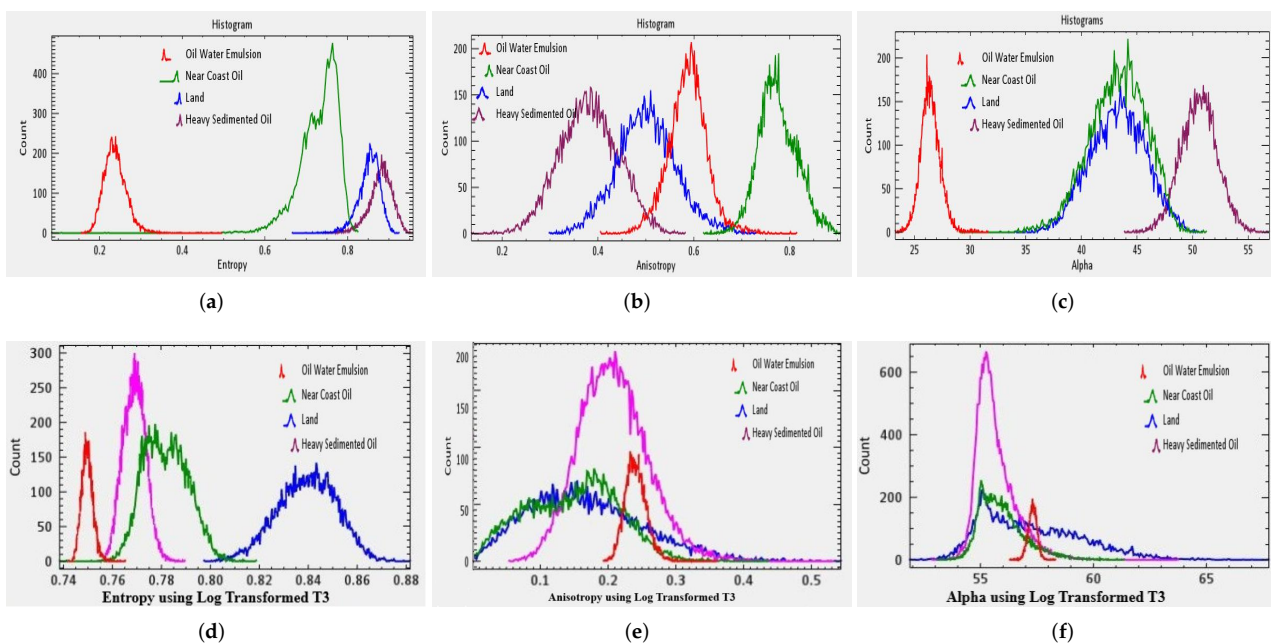


**Figure 11.** Statistical analysis of results of  $H/A/\alpha$  decomposition using conventional T3 and log transformed T3, i.e., Histogram of Entropy  $H$  (a,d), Anisotropy  $A$  (b,e) and Scattering Angle  $\alpha$  (c,f) for different patches showing ranges for Oil water Emulsion (Red), thick Oil (Green), Heavy Sedimented oil (Pink), Land/Mudflat (black).

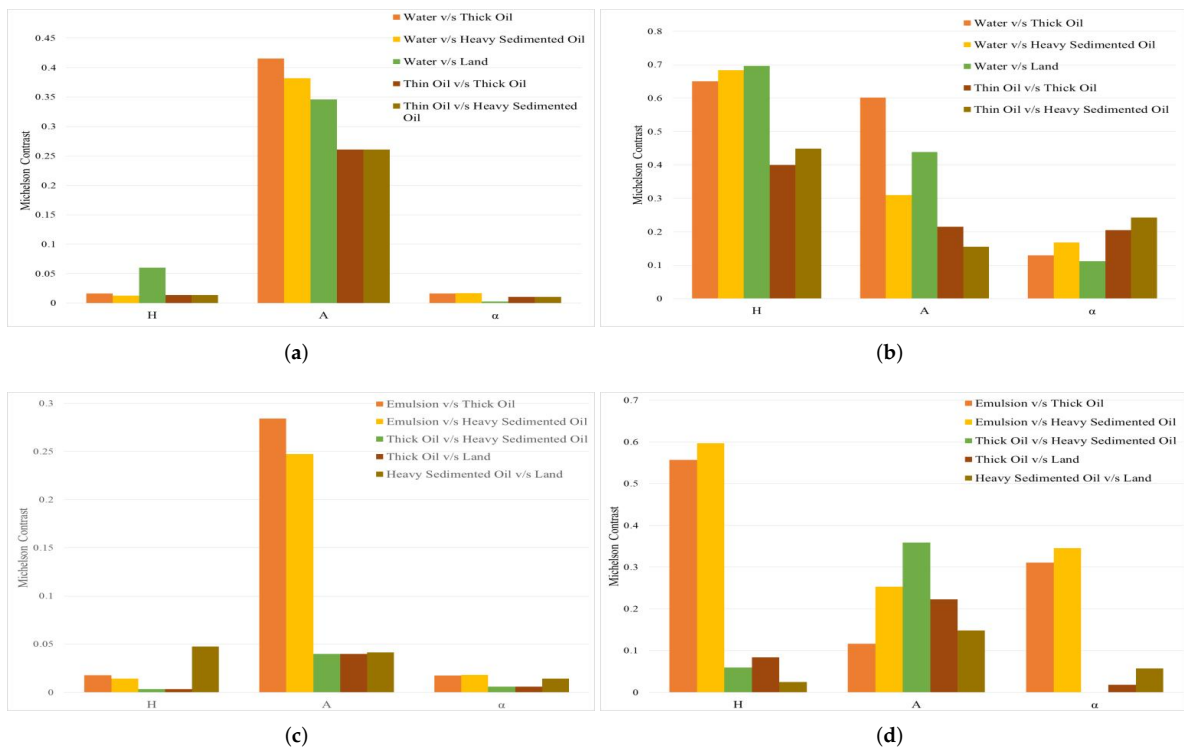


**Figure 12.** Michelson Contrast result analysis with respect to different types of polarimetric feature. For Conventional T3 (a) Different types of oil slick versus seawater& (c) Comparison of Different type Weathered Oil slick & look-alikes. For Proposed Log Transformed T3 (b) Different types of oil slick versus seawater& (d) Comparison of Different type Weathered Oil slick & look-alikes.

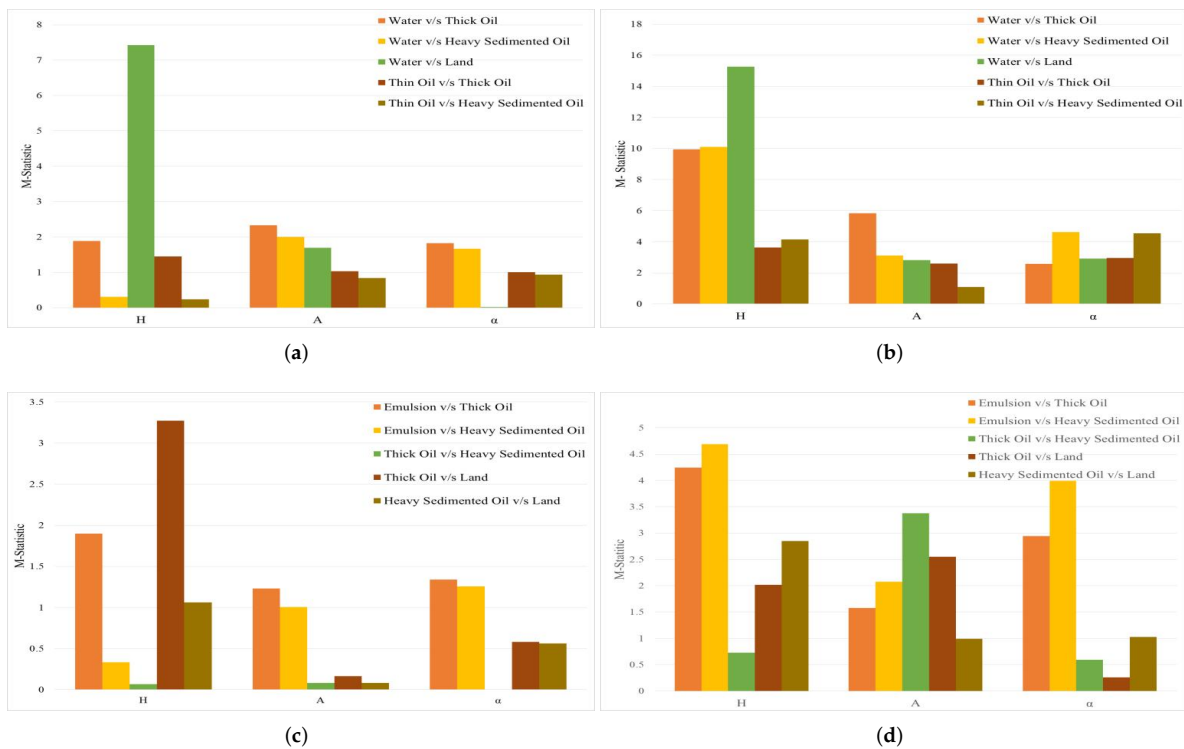


**Figure 13.** M-Statistic result analysis with respect to different types of polarimetric feature. For Conventional T3 (a) Different types of oil slick versus seawater& (c) Comparison of Different type Weathered Oil slick and look-alikes. For Proposed Log Transformed T3 (b) Different types of oil slick versus seawaterand (d) Comparison of Different type Weathered Oil slick and look-alikes.

#### 4.4. SVM Classification

SVM classification algorithm is majorly used for accuracy assessment and classification of the remote sensing data due to its important features such as self-adaptability, swift learning pace, and a limited requirement on training samples. Hence SVM is best suited here for the classification of the oil spill. The SVM classification has been carried out with 6 class ROI (Region of Interest) that includes Water, thin oil, Oil-Water Emulsion, Thick Oil, Heavy Sedimented Oil, and Land. The input features  $H$ ,  $A$ ,  $\alpha$  have been used here. We have optimized three hyper-parameters to achieve the best performance for oil spill characterization. The three major parameters include kernel, regularization parameter ( $C$ ), and kernel coefficient parameter ( $\Gamma$ ). The kernel is a core function that transforms the input space from a lower dimension to a higher dimension in a non-linear fashion. The regularization parameter ( $C$ ) is the penalty parameter that indicates the misclassification boundary of different classes. The kernel coefficient parameter ( $\Gamma$ ) indicates the distance impact on the line of different class separations. The best-case hyperparameters are Kernel-Sigmoid, Regularization Parameter( $C$ )-0.9 with pyramid level 3, and  $\Gamma$  value was set to 0.333. The SVM classification result for the  $H/A/\alpha$  decomposition algorithm using the proposed log-transformed T3 is shown in Figure 14. The researcher in [40] achieved an accuracy of 87% using SVM classification for oil spill detection using SAR images, while the researcher in [19] attained the kappa coefficient accuracy of 76% for discrimination of various types of oil slick based on its thickness. The overall accuracy of 97% is achieved with kappa coefficient 0.9607 using SVM classification for the proposed approach of log transformation of the coherency matrix for discrimination of various types of weathered oil using the  $H/A/\alpha$  decomposition algorithm, proving the significance of proposed approach over other existing algorithms.

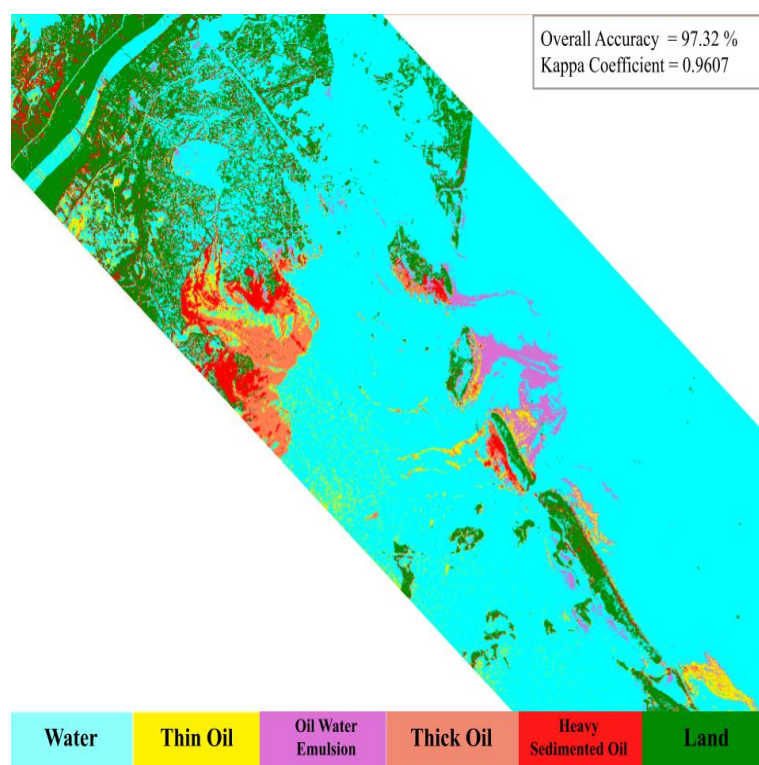


Figure 14. SVM Classification image for proposed log transformed approach.

#### 5. Conclusions

The advantage of log transformation to enhance the dark features of oil in the SAR image is used in this paper. Log transformation has been applied to each element of the coherency matrix to generate the log-transformed coherency matrix (T3) of the full polarimetric SAR image. The eigenvalue-eigenvector-based  $H/A/\alpha$  decomposition algorithm

analyzes the effect of the proposed log transformation. The proposed algorithm offers a major accuracy improvement in detecting various types of weathered oil spills on the ocean surface, significantly advancing the current state of the practice with an accuracy of 97%. Further, compared to the conventional approach, the land features are also distinguished with enhanced representation. The proposed algorithm can be further enhanced using the deep learning approach to classify various types of weathered oil spills efficiently.

**Author Contributions:** Conceptualization: K.P. and R.R.; writing—original draft preparation: M.B., Z.N. and S.T.; methodology: A.M. and R.R.; writing—review and editing: A.M. and A.B.; Investigation: K.P., M.S.R. and Z.N.; Supervision: M.B., R.R. and S.T.; Visualization: R.R., A.B. and A.M.; Software: S.T., M.S.R. and K.P. All authors have read and agreed to the published version of the manuscript.

**Funding:** The research work was carried out as a part of the ASAR L and S band project entitled “SAR Polarimetry for Detecting Ocean Surface Target” funded by Indian Space Research Organisation (ISRO) at Institute of Technology, Nirma University, Ahmedabad. And the APC was funded by the Subprogram 1.1. Institutional performance-Projects to finance excellence in RDI, Contract No. 19PFE/30.12.2021 and a grant of the National Center for Hydrogen and Fuel Cells (CNHPC)—Installations and Special Objectives of National Interest (IOSIN).

**Institutional Review Board Statement:** Not applicable.

**Informed Consent Statement:** Not applicable.

**Data Availability Statement:** No data is associated with this research work

**Conflicts of Interest:** The authors declare no conflict of interest.

## References

1. Transportation Research Board and National Research Council. *Oil in the Sea III: Inputs, Fates, and Effects*; National Academies Press (US): Washington, DC, USA, 2003.
2. Skrunes, S.; Brekke, C.; Eltoft, T. Characterization of marine surface slicks by radarsat-2 multipolarization features. *IEEE Trans. Geosci. Remote Sens.* **2014**, *52*, 5302–5319. [[CrossRef](#)]
3. Velotto, D.; Migliaccio, M.; Nunziata, F.; Lehner, S. Dual-polarized TerraSAR-X data for oil-spill observation. *IEEE Trans. Geosci. Remote Sens.* **2011**, *49*, 4751–4762. [[CrossRef](#)]
4. Kudryavtsev, V.N.; Chapron, B.; Myasoedov, A.G.; Collard, F.; Johannessen, J.A. On dual co-polarized SAR measurements of the ocean surface. *IEEE Geosci. Remote Sens. Lett.* **2012**, *10*, 761–765. [[CrossRef](#)]
5. Skrunes, S.; Brekke, C.; Eltoft, T.; Kudryavtsev, V. Comparing near-coincident C-and X-band SAR acquisitions of marine oil spills. *IEEE Trans. Geosci. Remote Sens.* **2014**, *53*, 1958–1975. [[CrossRef](#)]
6. ASCE Task Committee on Modeling of Oil Spills. State-of-the-art review of modeling transport and fate of oil spills. *J. Hydraul. Eng.* **1996**, *122*, 594–609. [[CrossRef](#)]
7. Jones, C.E.; Holt, B. Experimental L-band airborne SAR for oil spill response at sea and in coastal waters. *Sensors* **2018**, *18*, 641. [[CrossRef](#)]
8. Alpers, W.; Holt, B.; Zeng, K. Oil spill detection by imaging radars: Challenges and pitfalls. *Remote Sens. Environ.* **2017**, *201*, 133–147. [[CrossRef](#)]
9. Leifer, I.; Lehr, W.J.; Simecek-Beatty, D.; Bradley, E.; Clark, R.; Dennison, P.; Hu, Y.; Matheson, S.; Jones, C.E.; Holt, B.; et al. State of the art satellite and airborne marine oil spill remote sensing: Application to the BP Deepwater Horizon oil spill. *Remote Sens. Environ.* **2012**, *124*, 185–209. [[CrossRef](#)]
10. Al-Ruzouq, R.; Gibril, M.B.A.; Shanableh, A.; Kais, A.; Hamed, O.; Al-Mansoori, S.; Khalil, M.A. Sensors, features, and machine learning for oil spill detection and monitoring: A review. *Remote Sens.* **2020**, *12*, 3338. [[CrossRef](#)]
11. Masud, M.; Alshehri, M.; Alroobaea, R.; Mohammad, S. Leveraging Convolutional Neural Network for COVID-19 Disease Detection Using CT Scan Images. *Intell. Autom. Soft Comput.* **2021**, *29*, 1–13. [[CrossRef](#)]
12. Topouzelis, K.; Singha, S. Oil spill detection: Past and future trends. In Proceedings of the ESA Living Planet Symposium, Prague, Czech Republic, 9–13 May 2016; European Space Agency (Special Publication): Paris, France, 2016.
13. Zhang, Y.; Li, Y.; Lin, H. Oil-Spill Pollution Remote Sensing by Synthetic Aperture Radar. In *Advanced Geoscience Remote Sensing*; IntechOpen: London UK, 2014; pp. 27–50. [[CrossRef](#)]
14. Müllenhoff, O.; Bulgarelli, B.; Ferraro, G.; Perkovic, M.; Topouzelis, K.; Sammarini, V. Geospatial modelling of metocean and environmental ancillary data for the oil spill probability assessment in SAR images. *Remote Sens. Environ. Monit. Gis Appl. Geol. VIII* **2008**, *7110*, 71100R. [[CrossRef](#)]

15. Leifer, I.; Clark, R.; Jones, C.; Holt, B.; Svejksky, J.; Swayze, G. Satellite and airborne oil spill remote sensing: State of the art and application to the BP DeepWater Horizon oil spill. In Proceedings of the 34th AMOP Technical Seminar on Environmental Contamination and Response, Banff, AB, Canada, 4–6 October 2011; pp. 270–295.
16. Carvalho, G.d.A.; Minnett, P.J.; Ebecken, N.F.; Landau, L. Oil Spills or Look-Alikes? Classification Rank of Surface Ocean Slick Signatures in Satellite Data. *Remote Sens.* **2021**, *13*, 3466. [[CrossRef](#)]
17. Sun, S.; Hu, C. The challenges of interpreting oil–water spatial and spectral contrasts for the estimation of oil thickness: Examples from satellite and airborne measurements of the deepwater horizon oil spill. *IEEE Trans. Geosci. Remote Sens.* **2018**, *57*, 2643–2658. [[CrossRef](#)]
18. Garcia-Pineda, O.; Staples, G.; Jones, C.E.; Hu, C.; Holt, B.; Kourafalou, V.; Graettinger, G.; DiPinto, L.; Ramirez, E.; Streett, D.; et al. Classification of oil spill by thicknesses using multiple remote sensors. *Remote Sens. Environ.* **2020**, *236*, 111421. [[CrossRef](#)]
19. Li, G.; Li, Y.; Hou, Y.; Wang, X.; Wang, L. Marine Oil Slick Detection Using Improved Polarimetric Feature Parameters Based on Polarimetric Synthetic Aperture Radar Data. *Remote Sens.* **2021**, *13*, 1607. [[CrossRef](#)]
20. Cloude, S.R.; Pottier, E. A review of target decomposition theorems in radar polarimetry. *IEEE Trans. Geosci. Remote Sens.* **1996**, *34*, 498–518. [[CrossRef](#)]
21. Cloude, S.R.; Pottier, E.; Boerner, W. Unsupervised Image Classification using the Entropy/Alpha/Anisotropy Method in Radar Polarimetry. In Proceedings of the NASA-JPL, AIRSAR-02 Workshop, Pasadena, CA, USA, 4–6 March 2002; Volume 44, pp. 4–6.
22. Belore, R.; Trudel, K.; Morrison, J. Weathering, emulsification, and chemical dispersibility of Mississippi Canyon 252 crude oil: field and laboratory studies. In Proceedings of the International Oil Spill Conference Proceedings (IOSC), Virtual, 10–14 May 2011; American Petroleum Institute: Washington, DC, USA, 2011; Volume 2011, p. abs247.
23. Kolian, S.R.; Porter, S.A.; Sammarco, P.W.; Birkholz, D.; Cake, E.W.; Subra, W.A. Oil in the Gulf of Mexico after the capping of the BP/Deepwater Horizon Mississippi Canyon (MC-252) well. *Environ. Sci. Pollut. Res.* **2015**, *22*, 12073–12082. [[CrossRef](#)]
24. French-McCay, D.P.; Spaulding, M.L.; Crowley, D.; Mendelsohn, D.; Fontenault, J.; Horn, M. Validation of oil trajectory and fate modeling of the Deepwater Horizon oil spill. *Front. Mar. Sci.* **2021**, *8*, 136. [[CrossRef](#)]
25. An, W.; Cui, Y.; Yang, J.; Member, S. Three-Component Model-Based Decomposition for Polarimetric SAR Data. *IEEE Trans. Geosci. Remote Sens.* **2014**, *48*, 2732–2739. [[CrossRef](#)]
26. Freeman, A.; Member, S.; Durden, S.L. A Three-Component Scattering Model for Polarimetric SAR Data. *IEEE Trans. Geosci. Remote Sens.* **1998**, *36*, 963–973. [[CrossRef](#)]
27. Migliaccio, M.; Nunziata, F.; Buono, A. SAR polarimetry for sea oil slick observation. *Int. J. Remote Sens.* **2015**, *36*, 3243–3273. [[CrossRef](#)]
28. Tong, S.; Liu, X.; Chen, Q.; Zhang, Z.; Xie, G. Multi-feature based ocean oil spill detection for polarimetric SAR data using random forest and the self-similarity parameter. *Remote Sens.* **2019**, *11*, 451. [[CrossRef](#)]
29. Li, G.; Li, Y.; Liu, B.; Hou, Y.; Fan, J. Analysis of Scattering Properties of Continuous Slow-Release Slicks on the Sea Surface Based on Polarimetric Synthetic Aperture Radar. *ISPRS Int. J. -Geo-Inf.* **2018**, *7*, 237. [[CrossRef](#)]
30. Song, D.; Ding, Y.; Li, X.; Zhang, B.; Xu, M. Ocean oil spill classification with RADARSAT-2 SAR based on an optimized wavelet neural network. *Remote Sens.* **2017**, *9*, 799. [[CrossRef](#)]
31. Shamsudeen, T.Y. Advances in remote sensing technology, machine learning and deep learning for marine oil spill detection, prediction and vulnerability assessment. *Remote Sens.* **2020**, *12*, 3416.
32. Prajapati, K.; Prajapati, P.; Ramakrishnan, R.; Mahajan, A.; Bhavsar, M. Feature Combination of Pauli and H/A/Alpha Decomposition for Improved Oil Spill Detection Using SAR. In Proceedings of the International Conference on Recent Trends in Image Processing and Pattern Recognition, Aurangabad, India, 3–4 January 2020; pp. 134–147.
33. Minchew, B.; Jones, C.E.; Holt, B. Polarimetric analysis of backscatter from the deepwater horizon oil spill using L-band synthetic aperture radar. *IEEE Trans. Geosci. Remote Sens.* **2012**, *50*, 3812–3830. [[CrossRef](#)]
34. Angelliaume, S.; Dubois-Fernandez, P.C.; Jones, C.E.; Holt, B.; Minchew, B.; Amri, E.; Miegebielle, V. SAR imagery for detecting sea surface slicks: Performance assessment of polarization-dependent parameters. *IEEE Trans. Geosci. Remote Sens.* **2018**, *56*, 4237–4257. [[CrossRef](#)]
35. Singha, S.; Ressel, R.; Velotto, D.; Lehner, S. A Combination of Traditional and Polarimetric Features for Oil Spill Detection Using TerraSAR-X. *IEEE J. Sel. Top. Appl. Earth Obs. Remote Sens.* **2016**, *9*, 4979–4990. [[CrossRef](#)]
36. Singha, S.; Ressel, R. Offshore platform sourced pollution monitoring using space-borne fully polarimetric C and X band synthetic aperture radar. *Mar. Pollut. Bull.* **2016**, *112*, 327–340. [[CrossRef](#)]
37. Krestenitis, M.; Orfanidis, G.; Ioannidis, K.; Avgerinakis, K.; Vrochidis, S.; Kompatsiaris, I. Oil spill identification from satellite images using deep neural networks. *Remote Sens.* **2019**, *11*, 1762. [[CrossRef](#)]
38. Matias, Í.d.O.; Genovez, P.C.; Torres, S.B.; Ponte, F.F.d.A.; Oliveira, A.J.S.d.; Miranda, F.P.d.; Avellino, G.M. Improved Classification Models to Distinguish Natural from Anthropogenic Oil Slicks in the Gulf of Mexico: Seasonality and Radarsat-2 Beam Mode Effects under a Machine Learning Approach. *Remote Sens.* **2021**, *13*, 4568. [[CrossRef](#)]
39. Zhu, Q.; Zhang, Y.; Li, Z.; Yan, X.; Guan, Q.; Zhong, Y.; Zhang, L.; Li, D. Oil Spill Contextual and Boundary-Supervised Detection Network Based on Marine SAR Images. *IEEE Trans. Geosci. Remote Sens.* **2021**, *60*, 5213910. [[CrossRef](#)]
40. Mera, D.; Bolon-Canedo, V.; Cotos, J.M.; Alonso-Betanzos, A. On the use of feature selection to improve the detection of sea oil spills in SAR images. *Comput. Geosci.* **2017**, *100*, 166–178. [[CrossRef](#)]

41. Zhang, J.; Feng, H.; Luo, Q.; Li, Y.; Wei, J.; Li, J. Oil spill detection in quad-polarimetric SAR Images using an advanced convolutional neural network based on SuperPixel model. *Remote Sens.* **2020**, *12*, 944. [[CrossRef](#)]
42. Fornaro, G.; Verde, S.; Reale, D.; Pauciuolo, A. CAESAR: An approach based on covariance matrix decomposition to improve multibaseline-multitemporal interferometric SAR processing. *IEEE Trans. Geosci. Remote Sens.* **2015**, *53*, 2050–2065. [[CrossRef](#)]
43. Jones, C.E.; Minchew, B.; Holt, B.; Hensley, S. Studies of the Deepwater Horizon Oil Spill With the UAVSAR Radar. In *Monitoring and Modeling the Deepwater Horizon Oil Spill: A Record Breaking Enterprise*; Geophysical Monograph. No.195; American Geophysical Union: Washington, DC, USA, 2013; pp. 33–50. [[CrossRef](#)]
44. Svejkovsky, J.; Hess, M.; Muskat, J.; Nedwed, T.J.; McCall, J.; Garcia, O. Characterization of surface oil thickness distribution patterns observed during the Deepwater Horizon (MC-252) oil spill with aerial and satellite remote sensing. *Mar. Pollut. Bull.* **2016**, *110*, 162–176. [[CrossRef](#)]
45. Garcia-Pineda, O.; MacDonald, I.R.; Li, X.; Jackson, C.R.; Pichel, W.G. Oil spill mapping and measurement in the Gulf of Mexico with textural classifier neural network algorithm (TCNNA). *IEEE J. Sel. Top. Appl. Earth Obs. Remote Sens.* **2013**, *6*, 2517–2525. [[CrossRef](#)]
46. Xu, B.; Cui, Y.; Li, Z.; Zuo, B.; Yang, J.; Song, J. Patch Ordering-Based SAR Image Despeckling Via Transform-Domain Filtering. *IEEE J. Sel. Top. Appl. Earth Obs. Remote Sens.* **2015**, *8*, 1682–1695. [[CrossRef](#)]
47. Gonzalez, R.C.; Woods, R.E. *Digital Image Processing*; Pearson Education Inc.: Upper Saddle River, NJ, USA, 2002.
48. Sumaiya, M.N.; Kumari, R.S.S. Logarithmic mean-based thresholding for SAR image change detection. *IEEE Geosci. Remote Sens. Lett.* **2016**, *13*, 1726–1728. [[CrossRef](#)]
49. Kaufman, Y.J.; Remer, L.A. Detection of forests using mid-IR reflectance: an application for aerosol studies. *IEEE Trans. Geosci. Remote Sens.* **1994**, *32*, 672–683. [[CrossRef](#)]